URSI GASS 2021, Rome, Italy, 28 August - 4 September 2021

Analysis on the Relativistic Electron Precipitation in the Midnight Sector

L. Capannolo[(1)], W. Li[(1)], R. Millan[(2)], J. Sample[(3)], S. Shekhar[(4)], and N. Sivadas[(5)]
(1) Center for Space Physics, Boston University, Boston, Massachusetts, USA
(2) Dartmouth College, Hanover, New Hampshire, USA
(3) Montana State University, Bozeman, Montana, USA
(4) Auburn University, Auburn, Alabama, USA
(5) NASA's Goddard Space Flight Center, Greenbelt, Maryland, USA

Abstract

We analyze the precipitation of relativistic electrons occurring in the midnight sector, defined over 22–02 MLT. In the nightside, electron precipitation is primarily driven either by pitch angle scattering from interactions between electrons and plasma waves or by pitch angle scattering due to the stretching of magnetic field lines (also called "current sheet scattering"). We identified ~400 relativistic electron precipitation events and separated them into wave-driven (REPs) and CSS-driven (CSSs) events. Although REPs tend to occur at slightly lower L shells and CSSs are found at marginally higher L shells, there is not a clear separation in location between these two precipitation types. Furthermore, we show that REPs occur on smaller L shell scales at post-midnight and on wider L shell scales at pre-midnight, suggesting that the wave driver characteristics vary across midnight.

1 Introduction

One key loss mechanism of the energetic electrons (>10s keV) that populate the radiation belts is their precipitation into the upper atmosphere of Earth. The radiation belts dynamics is indeed governed by acceleration and loss processes driven by several mechanisms, such as radial transport and wave-particle interactions [1] [2]. Electron precipitation also affects the upper atmosphere of Earth by enhancing its ionization levels [3] and accelerating some chemical reactions that ultimately lead to ozone depletion [4]. A complete characterization of electron precipitation and its associated sources are still incomplete.

Previous studies that investigated on relativistic electron precipitation found that it is typically occurring from noon to post-midnight and over ~3–7 L shells [5] [6]. In this work, we focus our attention on the relativistic electron precipitation occurring in the local midnight sector (22–02 magnetic local time, MLT). The majority of the relativistic precipitation in this region was found to be correlated with stronger geomagnetic activity and field line stretching [7]. Although it is known that two of the potential candidates for such precipitation are field-line curvature scattering or wave-particle interactions [8] [9], their relative contribution to the detected precipitation is still undetermined. Solving this open question would shed light on the source of the relativistic electron precipitation observed in the local midnight sector. In this work, we use an algorithm to find relativistic precipitation events and analyze those in the midnight sector. Depending on the precipitation driver, the relativistic precipitation events have a different morphology, thus allow us to classify them into current sheet scattering-driven events (CSSs) and wave-driven events (REPs).

2 Data and Methodology

In this analysis, we use the electron flux data from the POES (Polar Orbiting Environmental Satellites) and MetOp (Meteorological Operations) satellites, funded by NOAA (National Oceanic and Atmospheric Administration) and EUMETSAT (European Organisation for the Exploitation of Meteorological Satellites) respectively. These satellites constitute a constellation of low-Earth-orbiting (altitudes ~800-850 km) spacecraft that cover a wide range of MLT sectors, providing measurements of both protons and electrons at two pointing directions and several energy channels. We use the 2s data from the MEPED (Medium Energy Proton and Electron Detector) instrument aboard. Electron fluxes are provided in four integral energy channels E1 (>30 keV), E2 (>100 keV), E3 (>300 keV), and E4 (>700 keV) [10] [11]. For both species, the detector has two view directions: one pointed at zenith (0° telescope) and one perpendicular to it (90° telescope). As a result, at mid-to-high latitudes and low 90°/0° ratios [12], POES allows to distinguish the precipitating population (0° telescope) from the trapped one (90° telescope).

In order to find the relativistic electron precipitation events, we only use the relativistic electron channel (E4, >700 keV) and implement an algorithm that identifies precipitation events at any location within 2.5–8.5 L shells, with the exception of the South Atlantic Anomaly (SAA, defined as in [13]). Specifically, an event is identified by one threshold on the 0° telescope E4 flux (E4 (0°) ≥ 727 $s^{-1}cm^{-2}sr^{-1}$, corresponding to 4 count/s) and a ratio E4 (0°)/E4 (90°) ≥ 0.4, indicating that at least 40% of the relativistic electrons are precipitating. The criterion

for ratio is used to filter out REP events that do not show significant electron precipitation. The extent in time and L shell of the relativistic precipitation event is found through a second threshold (E4 (0°) ≥ 545 $s^{-1}cm^{-2}sr^{-1}$, corresponding to 3 count/s), in a similar methodology as [6]. The L shell extent is set to at least 4 data points (6 s in duration) and at max 15 data points (28 s in duration). We considered data from all satellites (MetOp-01, MetOp-02, MetOp-03, NOAA-15, NOAA-16, NOAA-17, NOAA-18, NOAA-19) in the POES/MetOp constellation, from 01/2012 to 12/2020. The algorithm identified ~15,000 events with ~4,500 in the midnight sector (22–02 MLT).

3 Classification Between Wave-Driven Precipitation and CSS-Driven Precipitation

We visually inspected all 4,500 relativistic electron precipitation events found over 22–02 MLT and classified them into two main categories: events driven by wave-particle interactions (REPs) and events driven by current sheet scattering (CSSs). Specifically, we were able to separate REP events from CSSs because each of them has a very peculiar morphology.

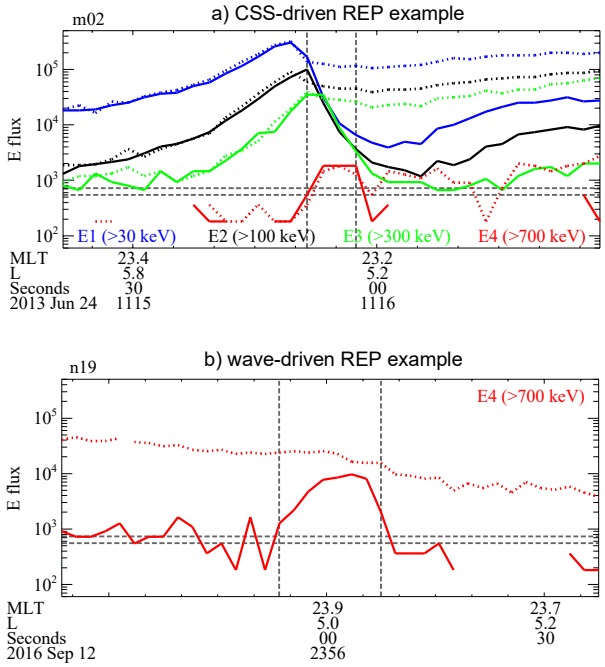

Figure 1: Example of a CSS-driven REP event (top, MetOp-02, m02) and a wave-driven REP event (bottom, NOAA-19, n19). The electron flux for the 0° (solid line) and 90° (dashed line) telescopes is color-coded by energy as indicated in the legends. The vertical dashed lines indicate the width of the identified event and the horizontal dashed lines indicate the two thresholds used.

Due to the mechanism that drives CSS events, the electron precipitation over 10s to 100s keV shows a clear energy dispersion as a function of L shell (Figure 1a). This is a typical feature found at the outer boundary of the outer radiation belt [14]. Higher energy electrons precipitate at lower latitudes (L shells), while lower energy electrons precipitate at higher latitudes (L shells). This is the result of a magnetic field line stretching in the nightside away from Earth: the field line curvature radius progressively decreases until it is first comparable to the gyroradius of more energetic electrons and later comparable to lower-energy electrons, driving precipitation of high-energy electron closer to Earth than that of lower-energy electrons. This is a well-known mechanism successfully studied also for protons [15] [16]. On the contrary, wave-driven REPs typically show an isolated relativistic electron precipitation, within the outer radiation belt (Figure 1b).

Only ~10% of the total number of precipitation events in the nightside were undoubtedly classifiable in these two categories (156 CSSs and 235 REPs) and we discarded any event that did not clearly fit in one category or the other. Out of the classified events, REPs contribute for ~60% of the total electron precipitation at midnight, however it is worth noting that this is not necessarily a conclusive result since ~90% of all the precipitation events at midnight did not clearly belong to one category or the other.

4 Distribution of the Relativistic Electron Precipitation

We show the distribution of all the relativistic electron precipitation events identified in an L-MLT plot in Figure 2a: REPs are indicated in red and CSSs are indicated in gray. The location of REPs is identified by the MLT and the L shell values averaged within the REP event width (two vertical bars in Figure 1b), while the location of CSSs is identified by the average MLT and the minimum L shell at which the energy dispersion in the electron flux is observed (right vertical bar in Figure 1a). The majority of the precipitation events occur between 4–7 L shells, with some outliers outside this range. It is overall expected to observe precipitation events within this L shell range since it typically identifies the outer radiation belt extent, where the majority of relativistic electrons reside. Overall, the distribution of REP events overlaps with that of the CSS events, suggesting that the drivers of these two phenomena coexist in the same region of space in the Earth's magnetotail. From the histograms of the distributions we can, however, observe some small differences: REPs tend to occur towards lower L shells, with some events extending to L~3 (Figure 2b), while the CSS events typically do not occur below L~4, but extend beyond L~7 (Figure 2c). Considering the distributions in MLT (not shown), the majority of REPs occur pre-midnight, while CSS events occur approximately at the same frequency pre- or post-midnight. For both categories, there are few events past MLT~1.

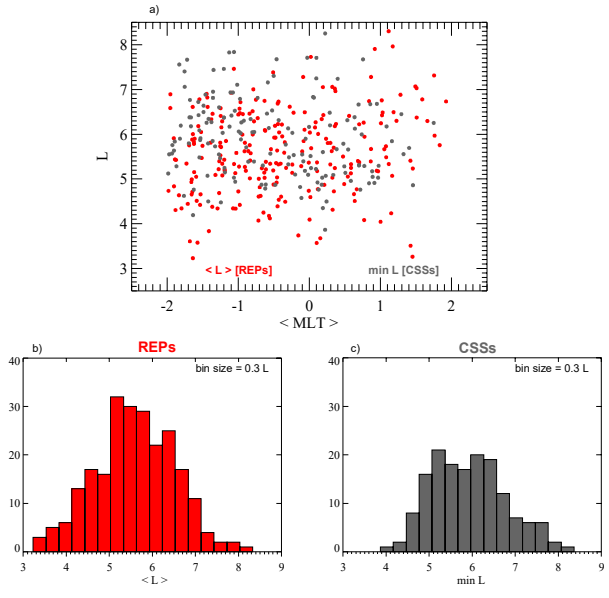

Figure 2: Distribution of the relativistic electron precipitation in the midnight sector. a) Scatter plot as a function of average MLT within the event boundaries (vertical lines in Figure 1) for REP (red) and CSS (black) events. REPs are located at the average L shell within the event boundaries. CSSs are located at the minimum L shell where the energy dispersion begins. Histograms of the REPs (b) and CSSs (c) are binned in 0.3 L intervals. The L shells are from the T05 model described in [17].

4.1 L-shell Extent of Wave-Driven REPs

In this section, we focus on the relativistic precipitation events driven by waves (REPs), thus those showing a clear isolated relativistic precipitation without any energy dispersion (Figure 1b). We analyze their spatial extent and distribution in MLT. Previous studies found that the precipitation in the nightside sector was overall broader (L shell extent ~ 1–2.5) than that observed elsewhere [6]. However, these studies were based on POES/MetOp data at 16s resolution, hence the lower resolution might have smoothed out smaller scale REPs. We report the L shell widths as a function of MLT location in Figure 3 for all the identified 235 REPs. The L shell width is defined by the second threshold used in the algorithm as described in Section 2: the dashed vertical bars in Figure 1b identify the width of the REP event. Our results show that the majority of REPs occurs on localized scales, from ~0.05 L up to ~0.8 L, with the majority of events at scales of ~0.1–0.3 L shells. Interestingly, pre-midnight events exhibit larger widths (up to ~0.7 L) compared to those post-midnight, which instead occur at smaller scales (~0.5 L) with the exception of two outliers. This suggests that favorable conditions for pitch angle scattering from wave-particle interactions or the specific characteristics of the wave drivers change across MLT~0.

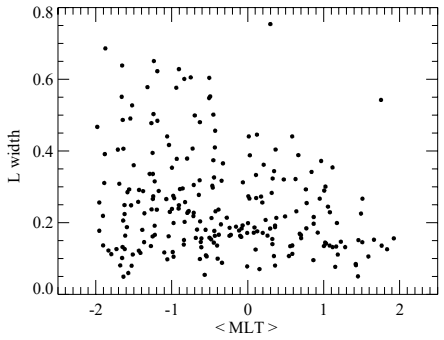

Figure 3: Scatter plot of the L shell widths of the wave-driven REP events as a function of average MLT within the event boundaries (vertical lines in Figure 1b).

5 Summary & Conclusions

In this work, we analyzed the precipitation of relativistic electrons (>700 keV) in the nightside sector from data taken by the POES/MetOp constellation. Through an algorithm and visual inspection, we identified a total of 391 relativistic precipitation events, which we classified into 235 (60%) wave-driven events (REPs) and 156 (40%) current sheet scattering-driven events (CSSs). The classification was possible because these two drivers determine a different morphology of the electron precipitation. Our results indicate that the two mechanisms coexist in the magnetotail and drive precipitation approximately in the same L and MLT region. However, REPs tend to occur at slightly lower L compared to CSSs, which instead are partly skewed towards higher L. These results are reasonable since CSS occurs when the magnetotail is more stretched (typically at higher L). Analyzing the L shell extent of the REP events, we found that the majority of this type of precipitation occurred on small scales (~0.1–0.3 L), overall smaller in the post-midnight sector and larger in the pre-midnight sector. These results might indicate that the characteristics of the wave drivers are different across the midnight sector.

In conclusion, further investigations are needed to reach closure of our understanding of nightside relativistic electron precipitation. For example, it would be important to understand if REP and CSS events occur during different geomagnetic conditions, what specific wave type drives the REPs, and if the REPs coincide with proton precipitation (thus are associated with electromagnetic ion cyclotron waves [18] [19]).

6 Acknowledgements

This research is supported by the NSF grants AGS-1723588 and AGS-2019950, the NASA grants 80NSSC20K0698 and 80NSSC20K1270, and the Alfred P. Sloan Research Fellowship FG-2018-10936. POES/MetOP data is available for download at https://satdat.ngdc.noaa.gov/sem/poes/data/processed/.

7 References

1. Reeves, G. D., K. L. McAdams, R. H. W. Friedel, and T. P. O'Brien (2003), Acceleration and loss of relativistic electrons during geomagnetic storms, Geophysical Research Letters, 30(10), 1529, doi:10.1029/2002GL016513.

2. Thorne, R. M. (2010), Radiation belt dynamics: The importance of wave - particle interactions, Geophysical Research Letters, 37, L22107, doi:10.1029/2010GL044990.

3. Ridley, A. J., Gombosi, T. I., and DeZeeuw, D. L. (2004), Ionospheric control of the magnetosphere: conductance, Ann. Geophys., 22, 567–584, https://doi.org/10.5194/angeo-22-567-2004.

4. Meraner, K. and Schmidt, H. (2018): Climate impact of idealized winter polar mesospheric and stratospheric ozone losses as caused by energetic particle precipitation, Atmospheric Chemistry and Physics, 18, 1079-1089, https://doi.org/10.5194/acp-18-1079-2018.

5. Comess, M. D., Smith, D. M., Selesnick, R. S., Millan, R. M., and Sample, J. G. (2013), Duskside relativistic electron precipitation as measured by SAMPEX: A statistical survey, J. Geophys. Res. Space Physics, 118, 5050– 5058, doi:10.1002/jgra.50481.

6. Shekhar, S., Millan, R., & Smith, D. (2017), A statistical study of the spatial extent of relativistic electron precipitation with polar orbiting environmental satellites. Journal of Geophysical Research: Space Physics, 122, 11,274–11,284. https://doi.org/10.1002/2017JA024716

7. Shekhar, S., Millan, R. M., & Hudson, M. K. (2018). A statistical study of spatial variation of relativistic electron precipitation energy spectra with Polar Operational Environmental Satellites. Journal of Geophysical Research: Space Physics, 123, 3349–3359. https://doi.org/10.1002/2017JA025041

8. Yahnin, A. G., T. A. Yahnina, N. V. Semenova, B. B. Gvozdevsky, and A. B. Pashin (2016), Relativistic electron precipitation as seen by NOAA POES, Journal of Geophysics Research Space Physics, 121, doi:10.1002/2016JA022765.

9. Smith, D. M., Casavant, E. P., Comess, M. D., Liang, X., Bowers, G. S., Selesnick, R. S., Clausen, L. B. N., Millan, R. M., and Sample, J. G. (2016), The causes of the hardest electron precipitation events seen with SAMPEX, J. Geophys. Res. Space Physics, 121, 8600– 8613, doi:10.1002/2016JA022346.

10. Evans, D. S., and M. S. Greer (2004), Polar Orbiting Environmental Satellite Space Environment Monitor-2: Instrument Descriptions and Archive Data Documentation, NOAA Tech. Mem. 93, version 1.4, Space Weather Predict. Cent., Boulder, Colo.

11. Yando, K., Millan, R. M., Green, J. C., & Evans, D. S. (2011). A Monte Carlo simulation of the NOAA POES medium energy proton and Electron detector instrument. Journal of Geophysics Research, 116, A10231. https://doi.org/10.1029/2011JA016671

12. Selesnick, R. S., Tu, W., Yando, K. B., Millan, R. M., & Redmon, R. J. (2020). POES/MEPED angular response functions and the precipitating radiation belt electron flux. Journal of Geophysical Research: Space Physics, 125, e2020JA028240. https://doi.org/10.1029/2020JA028240

13. M., Qin, Hudson, M., Millan, R., Woodger, L., & Shekhar, S. (2018). Statistical investigation of the efficiency of EMIC waves in precipitating relativistic electrons. Journal of Geophysical Research: Space Physics, 123, 6223– 6230. https://doi.org/10.1029/2018JA025419

14. Sivadas, N., Semeter, J., Nishimura, Y. T., & Mrak, S. (2019). Optical signatures of the outer radiation belt boundary. Geophysical Research Letters, 46, 8588– 8596. https://doi.org/10.1029/2019GL083908

15. Sergeev, V. A., Sazhina, E., Tsyganenko, N., Lundblad, J., & Søraas, F. (1983). Pitch angle scattering of energetic protons in the magnetotail current sheet as the dominant source of their isotropic precipitation into the nightside ionosphere. Planetary and Space Science, 31(10), 1147–1155.

16. Liang, J., Donovan, E., Spanswick, E., and Angelopoulos, V. (2013), Multiprobe estimation of field line curvature radius in the equatorial magnetosphere and the use of proton precipitations in magnetosphere - ionosphere mapping, J. Geophys. Res. Space Physics, 118, 4924– 4945, doi:10.1002/jgra.50454.

17. Tsyganenko, N. A., and M. I. Sitnov (2005), Modeling the dynamics of the inner magnetosphere during strong geomagnetic storms, Journal of Geophysics Research, 110, A03208, doi:10.1029/2004JA010798.

18. Capannolo, L., Li, W., Ma, Q., Shen, X. - C., Zhang, X. - J., Redmon, R. J., et al. (2019a). Energetic electron precipitation: Multievent analysis of its spatial extent during EMIC wave activity. Journal of Geophysical Research: Space Physics, 124. https://doi.org/10.1029/2018JA026291

19. Capannolo, L., Li, W., Spence, H., Johnson, A. T., Shumko, M., Sample, J., & Klumpar, D. (2021). Energetic Electron Precipitation Observed by FIREBIRD - II Potentially Driven by EMIC Waves: Location, Extent, and Energy Range from a Multi - Event Analysis. Geophysical Research Letters, 48, e2020GL091564. https://doi.org/10.1029/2020GL091564